Additive Manufacturing 97 (2025) 104596

Contents lists available at ScienceDirect

Additive Manufacturing

journal homepage: www.elsevier.com/locate/addma

Research paper

A physics-informed hybrid modeling framework for drop formation in drop-on-demand inkjet printing

Jie Wang [a,*], George T.-C. Chiu [b]

[a] Department of Chemical Engineering, Massachusetts Institute of Technology, 77 Massachusetts Ave, Cambridge, 02139, MA, USA
[b] School of Mechanical Engineering, Purdue University, 585 Purdue Mall, West Lafayette, 47907, IN, USA

ARTICLE INFO

Keywords:
Inkjet printing
Hybrid modeling
Equivalent circuits
Monte Carlo simulation
Parameter identification

ABSTRACT

Equivalent circuit models (ECMs) that capture low-order dynamics in drop formation are conducive to the integration of advanced control algorithms to enhance inkjet printing performance and the optimization of printhead design. However, the pinch-off of a drop from the nozzle transforms the continuous drop growth into a discrete event, where variations in drop characteristics are observed practically. To address this modeling discrepancy, this paper introduces a hybrid modeling framework that integrates continuous ECMs with data-driven adjusters. 3^{rd}-order ECMs are developed and validated to simulate the continuous drop growth within the nozzle, with parameters determined partially from sampled data and partially from prior knowledge of nozzle geometries and ink rheological properties. Data-driven adjusters and pinch-off estimates are then incorporated into ECM simulations to compensate for the variations occurring at the pinch-off, thereby improving the estimation accuracy for in-flight drop volume and jetting velocity. Cross-validation of the framework is performed using data from three different types of ink. Good agreement between simulations and experiments confirms the efficacy of this end-to-end hybrid modeling framework.

1. Introduction

The ability to precisely pattern functional materials on the substrate with predefined volume makes drop-on-demand (DoD) inkjet printing a high-efficiency tool for drug delivery [1–3], electronics fabrication [4,5], system functionalization [6,7] and 3D geometry construction [8–10]. Commercial DoD inkjet printheads typically provide users with several accessible control parameters to parameterize a constrained firing waveform. By tuning these parameters, users can regulate drop characteristics, such as drop volume and jetting velocity. Open-loop tuning has been widely adopted based on trial-and-error methods [11–15], numerical simulations [16–18], experimental data [19], wave propagation studies [20,21] and input–output models [22–24]. However, process and system uncertainties, including variations in nozzle size, supply pressure and temperature fluctuations, and ink aging and inhomogeneities, present challenges when printing in an open-loop manner. These uncertainties can significantly vary drop characteristics, thereby compromising the geometry and functionality of print products. Kamal et al. [4] and Tröndle et al. [9] reported high relative standard deviations (RSDs) in drop volume when printing electro-optic materials and bioinks, respectively. Empirical results also demonstrated notable spreads in drop volume and jetting velocity from printhead to printhead [25] and over time [26], even with well-tuned control parameters and the same material. To address these challenges, online parameter tuning algorithms or closed-loop control strategies have been developed by leveraging drop characteristics measured from vision systems [26–31]. When applying model-based tuning and control strategies, a high-fidelity model of drop formation – specifically, the formation of in-flight drop volume and drop jetting velocity – is required. It can provide insights into the relationship between manufacturer-provided control parameters and drop characteristics while facilitating integration with advanced control algorithms to ensure precise and robust printing processes.

First-principle-based models of drop formation in DoD inkjet printing have been developed over several decades. Fromm [32] pioneered the use of two-dimensional axisymmetric Navier–Stokes equations to investigate drop formation under different ink properties and pressure inputs. Xu et al. [33] numerically solved continuity and Navier–Stokes equations to explore the effect of ink properties and flow inputs with various driving frequencies on drop dynamics. By assuming axially-dependent fluid motion within the nozzle, one-dimensional models were proposed to examine drop characteristics under uncertainties, such as air bubble [34] and variations in nozzle diameter [35].

---

* Corresponding author.
E-mail address: jiew@mit.edu (J. Wang).

https://doi.org/10.1016/j.addma.2024.104596
Received 15 September 2024; Received in revised form 7 November 2024; Accepted 7 December 2024
Available online 14 December 2024

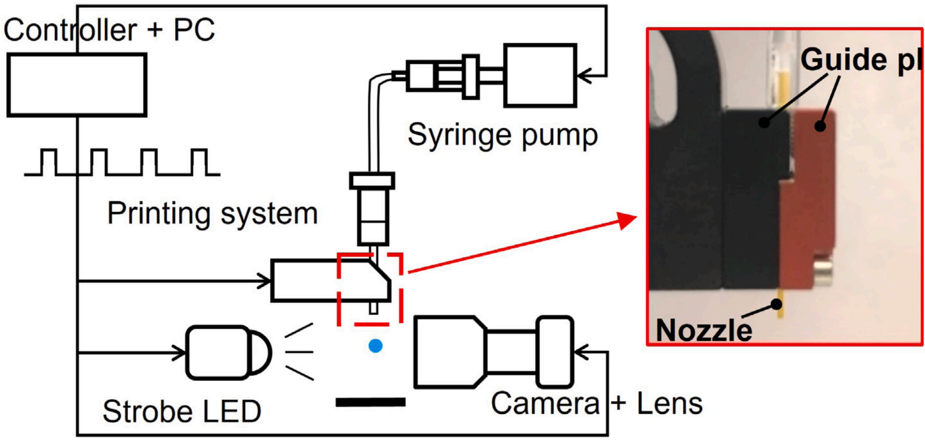

Fig. 1. Schematic of the printing system.

Equivalent circuit models (ECMs) have also been applied to discuss fluid behaviors regarding firing waveforms and printhead configurations [36–39]. Given that the characteristic dimension of a nozzle (in μm) is typically much smaller than the governing acoustic wavelength (in m) at hundreds or thousands of jetting frequencies, spatial and temporal variations of the fluid flow within the nozzle can be assumed to be decoupled. This enables the characterization of fluid motion using lumped elements [40]. By analogy, the lumped fluid elements and mechanical entities of the printhead can be represented by their electrical equivalents. In turn, the low-frequency dynamics of fluid flow within the nozzle can be effectively analyzed using an appropriately derived equivalent circuit model.

In recent years, data-driven approaches have been applied to predict drop characteristics, including regressions [26,29,30], neural networks [27,41–43], and other machine learning algorithms [44–47]. These models effectively map drop characteristics/output onto accessible control parameters/input, which can be readily synthesized for control design.

To address discrepancies between first-principles model predictions and actual system behaviors, hybrid models are proposed in additive manufacturing, where empirical data are incorporated to determine appropriate model structure and refine model prediction [48–51]. By integrating physical and mechanistic insights with data-driven adjustments, these hybrid models capture fundamental system behaviors and provide more accurate predictions under varying operating conditions.

In DoD inkjet printing, ECMs offer an efficient approach to capturing the growth of drop volume and velocity in the nozzle by providing insights into essential system dynamics beyond the processed data while minimizing computational load. However, accurately estimating in-flight drop volume and jetting velocity requires addressing discrepancies in drop characteristics at pinch-off, which are observed empirically in Fig. 6 and reported in [52–54]. These variations can be attributed to factors such as wetting properties at the nozzle tip and complex dynamics of the drop pinch-off [55–57], for which, to the best of the authors' knowledge, no relevant dynamic model is found in the literature. To resolve this modeling discrepancy, based on a data-driven modeling framework proposed by Wang and Chiu [52], in this study, we introduce physics-informed hybrid models for characterizing in-flight drop volume and jetting velocity in DoD inkjet printing. This hybrid modeling framework consists of two integral components: continuous ECMs and data-driven adjusters. The ECMs model drop growth within the nozzle before pinch-off, with parameters partially derived from historical data and partially informed by prior knowledge of nozzle geometries and ink rheological properties. They provide essential physical insights into drop formation, such as bandwidth and dynamics. The adjusters then complement the ECM simulations to account for the discrepancies at drop pinch-off. Through experimental validation with three different inks, the hybrid models demonstrate high accuracy in estimating in-flight drop volume and jetting velocity.

The remainder of this paper is organized as follows. An inkjet printing platform is introduced in Section 2, followed by the development of hybrid models. Section 4 covers data collection, as well as the evaluation and identification of these models. Model validation is presented in Section 5. Finally, Section 6 concludes the paper.

2. Printing system

As introduced in [26,29,30], the printhead in this study is a commercial squeeze-mode printhead (BioFluidix PipeJet P9, Freiburg, Germany) as shown in Fig. 1. The nozzle is a disposable pipe clamped between two guide plates. Fig. 2 illustrates the working mechanism of this printhead. The movement of a piezostack-driven piston governs the pipe deformation, where a rapid piston stroke expels an amount of ink out of the nozzle as a single drop within one firing cycle. The piston displacement $u(t)$ throughout a complete firing cycle follows a trapezoidal waveform, see Fig. 2, which is parameterized by stroke velocity u_1, piston stroke u_2, instroke velocity u_3, and stroke holding time t_H. The piece-wise function of the constrained waveform can be written as,

$$u(t,u_1,u_2,u_3,t_H)=\begin{cases} u_1\times t & 0\le t\le \frac{u_2}{u_1},\\ u_2 & \frac{u_2}{u_1}<t\le \frac{u_2}{u_1}+t_H,\\ u_2-u_3\times(t-(\frac{u_2}{u_1}+t_H)) & \frac{u_2}{u_1}+t_H<t\le \\ & \frac{u_2}{u_1}+t_H+\frac{u_2}{u_3},\end{cases} \tag{1}$$

where u_1 and u_2 are the user-accessible control parameters, and t is the time. The printhead is capable of firing drop volume up to 70 nl at a frequency up to hundreds of hertz with a 200-μm inner diameter nozzle.

In the printing platform, an imaging system comprising a strobe LED and a monochrome camera with a 1X telecentric lens is integrated to monitor drop behaviors. It has a resolution of 1.3 megapixels with a pixel size of 4.73 μm. A syringe pump is PID-controlled to regulate the back pressure at the reservoir. A trigger signal synchronizes the printhead, camera, and strobe LED through a myRIO FPGA (National Instruments).

3. Hybrid modeling strategy

A physics-informed hybrid modeling framework is introduced in this section to characterize the formation of a drop from its continuous growth within the nozzle to pinch-off, as illustrated in Fig. 3. Physics-based ECMs are developed to approximate the growing drop volume and flow rate. To address discrepancies in drop characteristics

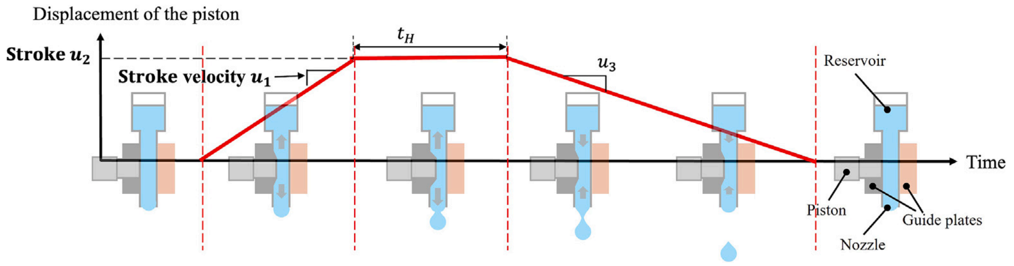

Fig. 2. Formation of a drop regarding piston displacements, represented by a parameterized firing waveform.

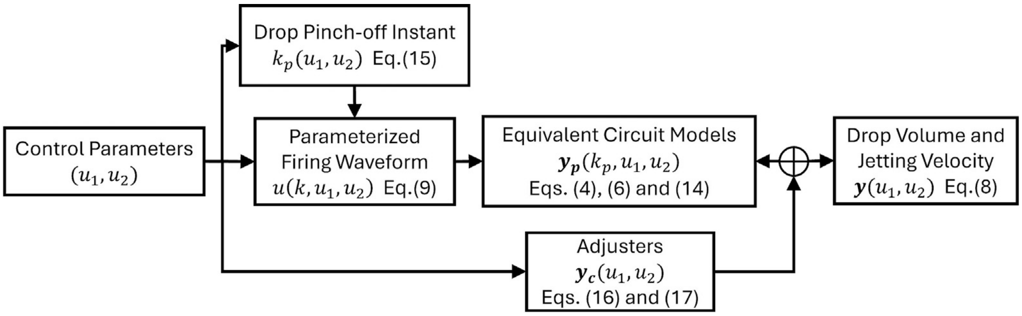

Fig. 3. Hybrid modeling framework of drop formation.

at pinch-off and improve estimations of in-flight drop volume and jetting velocity, volume and velocity adjusters are proposed to adjust the ECM-simulated results. Two user-adjustable control parameters (u_1, u_2) define the firing waveform, which is the input to ECMs, and approximate the pinch-off instant.

3.1. Equivalent circuit model

The nozzle is considered to be rigid to the fluid flow, with the motion of a piston causing two distinct fluid flows as shown in Fig. 2. One flow is directed towards the open end for drop formation while the other moves towards the reservoir. Given that the nozzle diameter, the dominant characteristic dimension, is much smaller than the acoustic wavelength at jetting frequencies of a few hundred hertz, the lumped elements can effectively describe the fluid motion within the nozzle. The speed of fluid flow in the nozzle is notably slower than the acoustic speed in the fluid, and the Reynolds number associated with the pipe flow is low. Thus, it is reasonable to assume that the fluid flow within the nozzle is incompressible, laminar, and fully developed [58]. An equivalent circuit model can be constructed by employing analogies between fluid properties and their electrical equivalents [59], as shown in Fig. 4.

According to the hydraulic-electric analogy, a pressure drop is analogous to a voltage drop, the volumetric flow rate to the electric current, and the hydraulic resistance to the electric resistance [59]. Hydraulic resistance R and inertance L are defined as

$$R = \frac{8\mu l}{\pi r^4} \text{ and } L = \frac{\rho l}{\pi r^2}, \tag{2}$$

where l is the length of the pipe with a radius r, μ is the fluid viscosity, and ρ is the fluid density.

L_a and R_a in Fig. 4 denote the mechanical inductance and loss, respectively, associated with the piston motion. The transformer represents the transfer from mechanical motion to fluid motion. A compliance ratio K_c relates the piston displacement $u(t)$ in Eq. (1) with the effective pressure V_s caused by piston force onto the fluid. I_N and I_R represent the two flows resulting from piston motion towards the open end and the reservoir, respectively. (L_N, R_N) and (L_R, R_R) are the fluid inertance and resistance towards the nozzle open end and the reservoir, respectively. To account for the effect of pressure on volume change at the meniscus, a compliance C_N is incorporated in the model. Compliance at the reservoir end is neglected, given the negligible volume change to the formation of a drop.

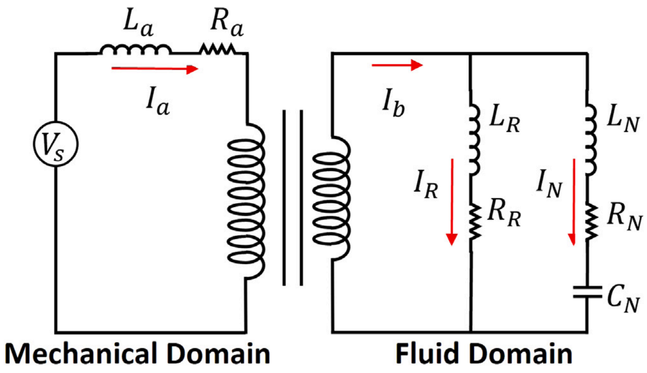

Fig. 4. Equivalent circuit model of the nozzle.

By assuming all $R's$, $L's$ and C_N are time-invariant, the following relations are obtained based on Kirchhoff's laws and Ohm's law,

$$\begin{aligned} &I_b = I_N + I_R, \\ &L_N \dot{I}_N + R_N I_N + \frac{1}{C_N}\int I_N dt = L_R \dot{I}_R + R_R I_R, \\ &V_s = L_a \dot{I}_a + R_a I_a, \quad \text{and} \\ &I_b = -I_a. \end{aligned} \tag{3}$$

Solving the flow rate I_N in Eq. (3) for the input V_s, replacing V_s with equivalent displacement $K_c u$, and converting the result to Laplace domain with an assumption of zero initial conditions, then it comes to

$$I_N(s) = \pi r^2 Y_p^{vel}(s) = -\frac{B_1 s + B_0}{A_3 s^3 + A_2 s^2 + A_1 s + A_0} sU(s), \tag{4}$$

where

$$\begin{aligned} A_3 &= C_N L_N L_a + C_N L_R L_a, \\ A_2 &= C_N L_a R_R + C_N L_a R_N + C_N L_N R_a + C_N L_R R_a, \\ A_1 &= C_N R_R R_a + C_N R_N R_a + L_a, \\ A_0 &= R_a,\ B_1 = K_c C_N L_R,\ \text{and}\ B_0 = K_c C_N R_R. \end{aligned} \tag{5}$$

The negative sign denotes the flow direction towards the nozzle end. $Y_p^{vel}(s)$ is the Laplace transform of average fluid velocity $y_p^{vel}(t)$.

The growing volume $y_p^{vol}(t)$ in Laplace domain can be represented by,

$$Y_p^{vol}(s) = \frac{1}{s} I_N(s) = -\frac{B_1 s + B_0}{A_3 s^3 + A_2 s^2 + A_1 s + A_0} U(s). \tag{6}$$

Eqs. (4) and (6) present 3rd –order models of the growing average velocity and drop volume, respectively, influenced by the firing waveform.

3.2. Data-driven models of pinch-off instant and adjusters

As discussed earlier, there are no dynamic models found in the literature that accurately represent variations in drop volume and jetting velocity at pinch-off. Similar to the approach in [52], this paper proposes data-driven approximations for pinch-off instant and adjustments for drop volume and velocity. These models adjust the results from the continuous ECMs for more accurate estimations of discrete in-flight drop volume and jetting velocity.

To establish an explicit correlation between input and output variables, polynomials of accessible control parameters $(u_1,\ u_2)$ are proposed as candidates for modeling the pinch-off instant k_p and volume and velocity adjusters $(y_c^{vol},\ y_c^{vel})$,

$$\begin{aligned} z(u_1, u_2) = {} & p_{0,0} + p_{1,0}u_1 + p_{0,1}u_2 + p_{2,0}u_1^2 + p_{1,1}u_1u_2 \\ & + p_{0,2}u_2^2 + \cdots + p_{n_1,0}u_1^{n_1} + p_{n_1-1,1}u_1^{n_1-1}u_2 \\ & + \cdots + p_{1,n_2-1}u_1u_2^{n_2-1} + p_{0,n_2}u_2^{n_2}, \end{aligned} \tag{7}$$

where $p_{i,j}$ represents the coefficient, $i = 0, 1, \ldots, n_1$ and $j = 0, 1, \ldots, n_2$, while n_1 and n_2 denote the orders for u_1 and u_2, respectively.

3.3. Hybrid modeling framework

By concatenating ECMs and adjusters as depicted in Fig. 3, a hybrid modeling framework is constructed,

$$\mathbf{y}(u_1, u_2) = \begin{bmatrix} y^{vol} \\ y^{vel} \end{bmatrix} = \mathbf{y_p}(k_p, u_1, u_2) + \mathbf{y_c}(u_1, u_2). \tag{8}$$

In Eq. (8), y^{vol} and y^{vel} are the in-flight drop volume and jetting velocity, respectively. $\mathbf{y_p}(k_p, u_1, u_2) = [y_p^{vol},\ y_p^{vel}]^T$, where y_p^{vol} is the grown drop volume achieved by simulating Eq. (6) at the pinch-off instant k_p and y_p^{vel} represents the average fluid velocity achieved by Eq. (4). $\mathbf{y_c}(u_1, u_2) = [y_c^{vol},\ y_c^{vel}]^T$ is the volume and velocity adjustments. Eq. (8) suggests that the discrete in-flight drop volume y^{vol} and drop jetting velocity y^{vel} can be projected onto the two user-adjustable control parameters $(u_1,\ u_2)$ of a firing waveform.

4. Model evaluation and identification

During printhead-ink calibration practice, experimental data are collected and processed. These data can be used to evaluate the structure of the developed ECMs and identify their unknown parameters. Additionally, these data allow for determining the appropriate polynomial orders for modeling the pinch-off instant and adjusters.

Table 1
List of ink properties and experimental parameters.

Name	DI Water	Color Ink	GW Mixture
Density (g/cm^3)	1.002	0.993	1.158
Viscosity (mPa s)	1.07	2.21	9.53
Surface Tension (mN/m)	73.24	28.72	67.87
Back Pressure (Pa)	0	−400	−100
Stroke Velocity u_1 Range (μm/ms)	60–75	50–80	70–100
Stroke Velocity u_1 Increment (μm/ms)	1.25	5	2.5
Stroke u_2 Range (μm)	20–35	20–35	25–35
Stroke u_2 Increment (μm)	1.25	1.25	1.25

4.1. Experimental setup and data collection

Three inks were tested with the PipeJet printhead: deionized (DI) water, pigmented color ink, and glycerol–water (GW) mixture composed of 60 $wt\%$ glycerol and 40 $wt\%$ DI water, see Table 1. They represent densities, viscosities, and surface tensions widely used in DoD inkjet printing. Following the printhead-ink calibration procedure detailed in [29], a set of experiments was conducted in printable regions defined by control parameters u_1 and u_2 as shown in Table 1 without exhibiting abnormal jetting behaviors such as satellite drops and unstable tails. More than two hundred drops were jetted at each combination of control parameters $(u_1,\ u_2)$. These drops were sequentially imaged at strobe intervals of 10 μs from the initialization of a drop firing trigger until the instant when a drop exited the field of view.

4.1.1. Data of volume and velocity

Fig. 5 shows several drop images at different strobe delays with respect to the initialization of a firing trigger. Meniscus is initially formed at the nozzle tip, see Fig. 5a. After the printhead receives a firing waveform signal, drop volume continues growing until a neck appears and shrinks as shown in Fig. 5b-f. Shortly after 1000 μs, a distinct drop is pinched off from the nozzle tip, see Fig. 5g.

In-flight drop volumes and jetting velocities are estimated using the methods detailed in [29]. By assuming that the nozzle and meniscus are rotationally symmetric to the axis of symmetry, the growing drop volume before pinch-off can be calculated by subtracting the initial meniscus volume in Fig. 5a from the following estimates. The average flow velocity is approximated by dividing the drop volume growth rate by the nozzle's cross-sectional area.

Figs. 6(a) and 6(b) show drop volumes and velocities of color ink for seven firing waveforms with the same stroke velocity u_1 and different strokes u_2. Solid color lines are the firing waveforms. Color circles represent the sampled volumes and average velocities, respectively. Filled color circles with error bars at the end denote the means and standard deviations of in-flight drop volumes and jetting velocities. The waveforms are delayed by 220 μs from the initialization of a drop firing trigger for comparison. Fig. 6(a) shows that after an approximately 220 μs delay, drop volume shows linear growth until reaching its maximum. Piston retraction decelerates volume growth afterward by pulling the volume back until a certain amount of volume is pinched off from the nozzle tip, forming a distinct characteristic drop. The results in Fig. 6(a) reveal that the in-flight drop volumes are larger than the drop volumes grown right before the pinch-off. Fig. 6(a) also highlights a proportional correlation between drop volume and stroke u_2.

Drop formation of color ink under firing waveforms with a constant stroke u_2 and four different stroke velocities u_1 is illustrated in Figs. 6(c) and 6(d). In Fig. 6(c), it is observed that after 220 μs, drop volume grows at a rate proportional to the stroke velocity u_1 until it reaches the maximum before decaying to pinch-off. Volume differences at the pinch-off are more intricate. At higher u_1, the pinch-off location is closer to the nozzle end, resulting in a larger in-flight drop due to the inclusion of additional meniscus volume. Conversely, with lower flow forwarding momentum, the pinch-off occurs further away from the nozzle, leaving

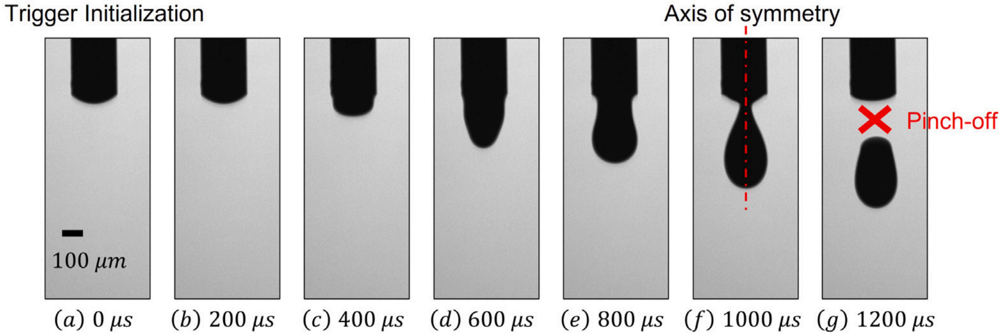

(a) 0 μs (b) 200 μs (c) 400 μs (d) 600 μs (e) 800 μs (f) 1000 μs (g) 1200 μs

Fig. 5. Sequential images of drop formation at different strobe delays.

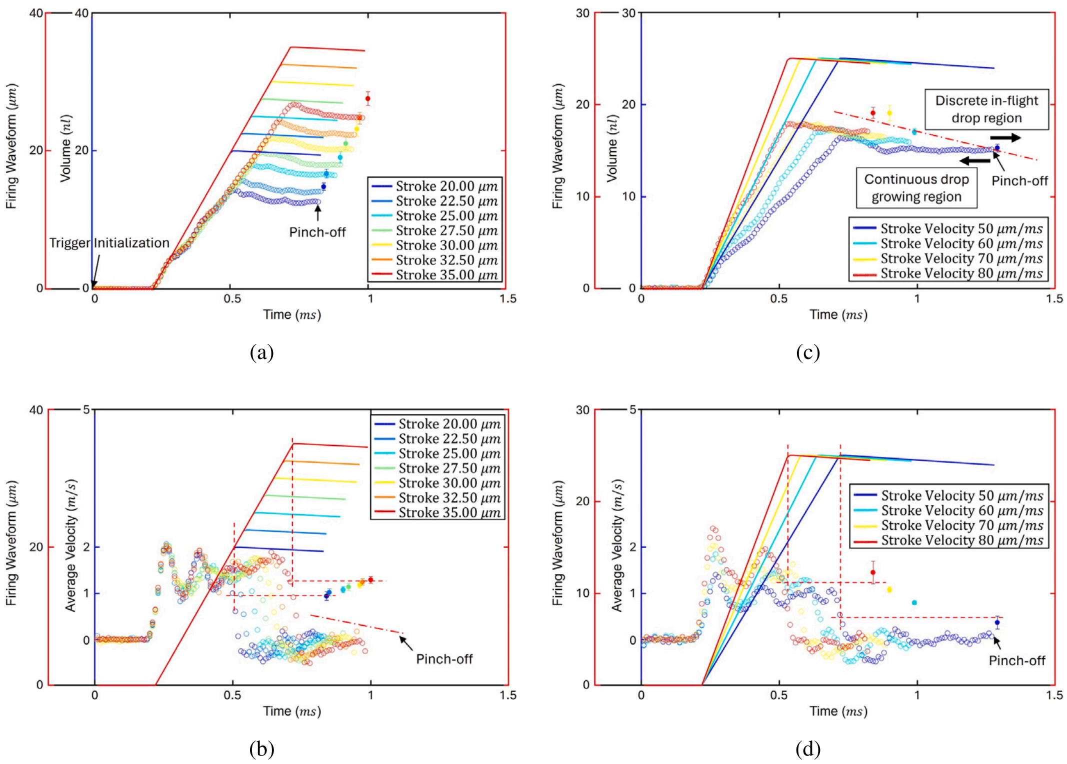

(a) (c) (b) (d)

Fig. 6. (a) Volumes and (b) average velocities of color ink at stroke velocity $u_1 = 70$ μm/ms and various strokes u_2. (c) Volumes and (d) average velocities of color ink at various stroke velocities u_1 and stroke $u_2 = 25$ μm. Solid color lines are the firing waveforms. Associated color circles represent growing drop volumes and average velocities at the nozzle. Associated filled color circles with error bars denote the means and standard deviations of in-flight drop volumes and jetting velocities. The waveforms are delayed by 220 ms from the initialization of a drop firing trigger for comparison.

a portion of the grown volume to remain at the meniscus and resulting in a smaller volume being pinched off. The results in Figs. 6(c) and 6(d) also suggest that stroke velocity u_1 primarily influences drop jetting velocity and has less degree of control over drop volume.

In Figs. 6(b) and 6(d), it is noteworthy that the drop jetting velocity is closely related to the average fluid velocity that occurs at the maximum stroke of the piston. This suggests that in-flight drops preserve a considerable portion of the kinetic energy from piston motion. Similar drop formation characteristics are observed with other inks and operating conditions.

4.1.2. Data of pinch-off instant and differences in volume and velocity

Based on the data illustrated in Fig. 6, the dataset of pinch-off instants at control parameter pairs $(u_1,\ u_2)$ is processed by identifying the moment when a drop separates from the meniscus in the drop image. The volume difference at pinch-off is computed by subtracting the grown drop volume right before pinch-off from the in-flight drop volume. The velocity variation is determined by subtracting the average fluid velocity occurring at the maximum stroke from the drop jetting velocity.

4.2. Evaluation of equivalent circuit models

As shown in Eqs. (4) and (6), third-order models with lumped physical properties are proposed to represent the growing drop characteristics before pinch-off. Data collected at each combination of control parameters $(u_1,\ u_2)$ can be used to evaluate the structure of the derived ECM.

Given that drop volumes are collected every $t_s = 10$ μs, the firing waveform presented in Eq. (1) is discretized accordingly with factory-preset values of $u_3 = 2$ μm/ms and $t_H = 20$ μs, as follows,

$$u_p(k, k_p, u_1, u_2) = \begin{cases} u_1 \times k t_s & 0 \le k \le \frac{u_2}{u_1 t_s}, \\ u_2 & \frac{u_2}{u_1 t_s} < k \le \frac{u_2}{u_1 t_s} + 2, \\ u_2 - 2 \times (k - (\frac{u_2}{u_1 t_s} + 2)) t_s & \frac{u_2}{u_1 t_s} + 2 < k \le k_p, \\ \text{Not applicable} & k_p \le k, \end{cases} \tag{9}$$

Table 2

Statistics of strictly proper ARX models at $n_k = 22$ for color ink.

n_a	n_b	Training Data		Validation Data	
		RMSE (nl)	Fit Percent (%)	RMSE (nl)	Fit Percent (%)
2	1	1.73	77.5	1.71	77.4
3	1	1.43	81.2	1.42	81.1
4	1	1.43	81.2	1.42	81.1
5	1	1.44	81.1	1.43	81.0
6	1	1.44	81.1	1.43	81.0
7	1	1.44	81.2	1.42	81.0
3	2	0.71	90.9	0.68	90.8
4	2	0.68	91.4	0.65	91.2
5	2	0.63	92.1	0.60	91.9
6	2	0.59	92.6	0.56	92.5
7	2	0.57	92.8	0.55	92.7
4	3	0.68	91.4	0.65	91.2
5	3	0.63	92.1	0.60	91.9
6	3	0.58	92.6	0.56	92.5
7	3	0.57	92.8	0.54	92.7
5	4	0.63	92.1	0.60	91.9
6	4	0.58	92.7	0.56	92.5
7	4	0.56	92.9	0.54	92.8

Table 3

Identified parameters from datasets of color ink.

	K_c($\times10^{-7}$) (kg/ (m^2 s^2))	R_a($\times10^{-12}$) (kg/(m^4 s))	L_a ($\times10^{-13}$) (kg/m^4)	C_N ($\times10^{-20}$) ((m^4 s^2)/kg)
Mean	−6.77	14.02	4.01	1.11
EB[a]	0.082	0.056	0.016	0.004

[a] EB is the error bound of a 95% confidence interval.

where k denotes the sampling instant. k_p represents the instant of a drop pinched off from the nozzle, which also is the final moment that piston motion influences the drop growth.

Similar to [52], a collection of ARX (Autoregressive with Extra Input) models is constructed by varying the polynomial orders (n_a, n_b) and delay n_k. By using firing waveforms $u_p(k, k_p, u_1, u_2)$ in Eq. (9) at different pairs of control parameters (u_1, u_2) (input data), associated collected drop volumes $y_p^{vol}(k)$ (output data), and identified pinch-off instants k_p, 10-fold cross-validation is employed to evaluate the model structure. Root mean square error (RMSE) and fit percent are used to measure the quality of the ARX models [60].

Table 2 lists the results of several strictly proper ARX models assessed with color ink data. Although higher-order ARX models have a modest improvement in approximation accuracy, an ARX model with $n_a = 3$, $n_b = 2$, and $n_k = 22$ can achieve comparable RMSE and fit percent metrics with a simpler structure. In turn, these results confirm the efficiency of the third-order ECM proposed in Section 3.1 in modeling the drop growth within the nozzle and 220 μs input delay shown in Fig. 6.

4.3. Parameter identification of equivalent circuit models

In the proposed ECM, hydraulic equivalents can be calculated using Eq. (2), if the values of nozzle geometries and ink rheological properties are known. Quantities, such as L_a, R_a, and K_c, are not typically included as specifications in commercial printheads. Calculation of compliance C_N remains challenging due to complex interactions among back pressure, surface tension, and the dynamic nature of the ink flow. Alternatively, these parameters can be approximated from available empirical data.

Identifying these physical properties from continuous-time models is preferred due to their continuous representation of physical laws in nature. Equivalent continuous-time models are achievable through converting the identified ARX model in Section 4.2. However, there exist technical difficulties in specifying the physical attributes from these converted continuous-time models, such as mismatches of zeros and sampling-rate dependence [61,62]. In this study, given the validated ECM structure and calculated hydraulic equivalents, a least squares method is employed to estimate L_a, R_a, K_c, and C_N from the derivative-approximated ECM.

A differentiation operator $p = \frac{d}{dt}(\cdot)$ is used to rewrite the resulting equation after applying the inverse Laplace transform to Eq. (6),

$$p^3 y_p^{vol}(t) = \varphi^T \theta, \tag{10}$$

where $\varphi^T = [-p^2 y_p^{vol}(t),\ -p y_p^{vol}(t),\ -y_p^{vol}(t),\ -pu(t),\ -u(t)]$ and $\theta = [A_2/A_3,\ A_1/A_3,\ A_0/A_3,\ B_1/A_3,\ B_0/A_3]^T$. A difference operator, or a delta operator [63], is then applied to approximate the differentiation. Eq. (10) can be written as

$$\hat{y}_p^{vol}(k) = \varphi^T(k)\theta, \tag{11}$$

where $\varphi^T(k) = [y_p^{vol}(k-1),\ y_p^{vol}(k-2),\ y_p^{vol}(k-3),\ u(k-2),\ u(k-3)]$. θ is

$$\theta = \Big[\ 3 - h\frac{A_2}{A_3},\ -3 + 2h\frac{A_2}{A_3} - h^2\frac{A_1}{A_3},$$

$$1 - h\frac{A_2}{A_3} + h^2\frac{A_1}{A_3} - h^3\frac{A_0}{A_3},\ -h^2\frac{B_1}{A_3},\ h^2\frac{B_1}{A_3} - h^3\frac{B_0}{A_3}\ \Big]^T,$$

where h is the sampling subinterval.

By applying the final value theorem to Eq. (6) under a step input with amplitude K_{ss}, we have

$$\begin{aligned}\lim_{t\to\infty} y_p^{vol}(t) &= \lim_{s\to 0} s\left(-\frac{B_1 s + B_0}{A_3 s^3 + A_2 s^2 + A_1 s + A_0}\right)\frac{K_{ss}}{s} \\ &= -K_{ss}\frac{B_0}{A_0} = -K_{ss}\frac{K_c C_N R_R}{R_a}.\end{aligned} \tag{12}$$

Eq. (12) suggests

$$K_c = -\frac{y_{p,ss}^{vol} R_a}{K_{ss} C_N R_R}, \tag{13}$$

where $y_{p,ss}^{vol}$ is the steady-state volume achieved under a stroke of K_{ss}. By substituting Eq. (13) into θ, the parameters R_a, L_a and C_N can be approximated by minimizing the objective function J,

$$J = \frac{1}{N}\sum_{k}^{N}\left(y_p^{vol}(k) - \hat{y}_p^{vol}(k)\right)^2.$$

To enhance the estimation accuracy of ECMs for the grown drop volume at pinch-off, $y_{p,ss}^{vol}$ and K_{ss} used in the optimization above are the grown volume at pinch-off from the experimental data and the corresponding piston displacement. In turn, K_c is computed with the approximated R_a and C_N through Eq. (13).

Table 3 presents the mean and error bound of a 95% confidence interval for each parameter. With these values, the coefficients of ECMs in Eq. (4) and (6) for the color ink are given by:

$$\begin{aligned}&A_3 = 10.01 \times 10^{-25}_{(\pm0.16\times10^{-28})},\ A_2 = 15.42 \times 10^{-22}_{(\pm0.24\times10^{-25})},\\ &A_1 = 4.01 \times 10^{-13}_{(\pm1.59\times10^{-15})},\ A_0 = 14.02 \times 10^{-12}_{(\pm0.56\times10^{-13})},\\ &B_1 = -2.70 \times 10^{-19}_{(\pm1.31\times10^{-23})},\\ &B_0 = -9.49 \times 10^{-18}_{(\pm4.59\times10^{-22})},\end{aligned} \tag{14}$$

where subscripts are the error bounds of 95% confidence intervals.

Remark 1. As discussed in [61,62], pre-filtering schemes can be employed to address the bias on identified parameters resulting from least squares, which is caused by measurement noise. No prefilters are used in this work since the data are clean and informative in presenting each complete drop-growing cycle, as seen in Figs. 6(a) and 6(c). Rather, influences of noise and process uncertainty during data collection can be mitigated by averaging the parameters estimated from various experimental datasets.

Table 4
Statistics of polynomial models for pinch-off instants in color ink (instants are rounded off to their nearest greater or equal integer).

Order	Training Data RMSE (Instants)	Validation Data RMSE (Instants)
$n_1 = 1,\ n_2 = 1$	7	7
$n_1 = 1,\ n_2 = 2$	7	7
$n_1 = 1,\ n_2 = 3$	7	7
$n_1 = 2,\ n_2 = 1$	4	4
$n_1 = 2,\ n_2 = 2$	4	4
$n_1 = 2,\ n_2 = 3$	4	4

Table 5
Statistics of polynomial models for drop volume adjustments in color ink.

Order	Training Data RMSE (nl)	Validation Data RMSE (nl)
$n_1 = 1,\ n_2 = 1$	1.02	0.91
$n_1 = 1,\ n_2 = 2$	1.03	0.91
$n_1 = 1,\ n_2 = 3$	1.04	0.86
$n_1 = 2,\ n_2 = 1$	1.03	0.92
$n_1 = 2,\ n_2 = 2$	1.03	0.93
$n_1 = 2,\ n_2 = 3$	1.02	0.94

4.4. Evaluation and identification of models for pinch-off instant and adjusters

Using the color ink data detailed in Section 4.1.2, regression and 10-fold cross-validation are employed to determine the appropriate orders $(n_1,\ n_2)$ for approximating pinch-off instants k_p and adjusters $\mathbf{y_c} = [y_c^{vol}, y_c^{vel}]^T$, as well as to estimate the model coefficients. RMSE is utilized to evaluate these model candidates.

4.4.1. Pinch-off instants

The cross-validation results of several polynomials are shown in Table 4. A linear model $(n_1 = 1, n_2 = 1)$ can approximate an acceptable pinch-off instant with a simpler structure. The identified model is

$$k_p(u_1, u_2) = 163.1_{(\pm 15.4)} - 1.40_{(\pm 0.17)} u_1 + 1.02_{(\pm 0.33)} u_2. \tag{15}$$

4.4.2. Adjusters of drop volume

Table 5 shows RMSEs of several polynomials used to model the difference in drop volume, regarding training and validation data. A linear model comes to a simple and satisfactory representation of the drop volume adjuster $y_c^{vol}(u_1, u_2)$,

$$y_c^{vol}(u_1, u_2) = 0.16_{(\pm 1.87)} + 0.014_{(\pm 0.021)} u_1 + 0.0037_{(\pm 0.0454)} u_2. \tag{16}$$

4.4.3. Adjusters of drop jetting velocity

In Table 6, RMSEs of several drop jetting velocity adjusters are presented, which are trained and validated with color ink data, respectively. A linear model can achieve a comparable RMSE with a simpler structure compared to higher-order polynomials,

$$y_c^{vel}(u_1, u_2) = -0.155_{(\pm 0.300)} + 0.0025_{(\pm 0.0034)} u_1 + 0.0008_{(\pm 0.0072)} u_2. \tag{17}$$

5. Model validation

As outlined in Fig. 3, although continuous ECMs and data-driven adjusters have been individually evaluated with their respective experimental data, variability in the parameters of each model introduces uncertainty into the hybrid framework, affecting the accuracy of in-flight drop volume and jetting velocity estimations. To assess the impact of these parameter uncertainties on the framework, Monte Carlo simulations are performed.

Table 6
Statistics of polynomial models for drop jetting velocity adjustments in color ink.

Order	Training Data RMSE (m/s)	Validation Data RMSE (m/s)
$n_1 = 1,\ n_2 = 1$	0.15	0.16
$n_1 = 1,\ n_2 = 2$	0.15	0.16
$n_1 = 1,\ n_2 = 3$	0.16	0.16
$n_1 = 2,\ n_2 = 1$	0.15	0.16
$n_1 = 2,\ n_2 = 2$	0.15	0.16
$n_1 = 2,\ n_2 = 3$	0.16	0.16

5.1. Simulation setup

Control parameters $(u_1,\ u_2)$ are user-chosen to construct a firing waveform through Eq. (9). With these control parameters, 10000 pinch-off instants are estimated by combining 100 values randomly sampled from the interval of the constant term with 10 values from the interval of each coefficient of Eq. (15). To reduce the simulation load, the pinch-off instant estimated by the nominal coefficients is employed to truncate the firing waveform, which is the input to the ECMs.

With the truncated firing waveform, 10000 ECMs are simulated for volume and velocity growth, respectively, where 10 values of each of K_c, R_a, L_a, and C_N are randomly sampled from their respective confidence intervals as listed in Table 3 and combined. Using the control parameters, 10000 volume and jetting velocity adjustments are also sampled by randomly drawing 100 values of the constant term combined with 10 values of each coefficient from Eqs. (16) and (17). As specified in Eq. (8), in-flight drop volumes are estimated by adding these 10000 volume adjustments to the grown drop volume at pinch-off for each of the 10000 simulated ECM responses. Average velocities of these 10000 responses occurring at the maximum stroke of the truncated firing waveform are identified, each of which is subsequently compensated by the 10000 velocity adjustments to estimate the drop jetting velocity.

5.2. Validation with data of color ink

Following the procedure outlined in Section 4.1, drop volumes and velocities of color ink at control parameters ($u_1 = 70$ μm/ms, $u_2 = 25$ μm) are collected and used to validate the framework. In Figs. 7(a) and 7(b), the responses of ECMs with nominal coefficients specified in Eq. (14) are plotted in red solid lines, while experimental data are presented in black solid lines. The associated red shades denote the ranges of the 10000 simulated ECM responses. The red dots denote the mean values of these 100000000 in-flight drop volumes and jetting velocities, with associated variabilities in red shades. The mean values of measured in-flight drop volumes and drop jetting velocities are depicted by black dots with gray shades representing their spreads.

The purple shading in Fig. 7(a) represents a distribution of the 10000 pinch-off instants. The wide spread is attributed to the large confidence intervals of model parameters in Eq. (15). Collecting more data and incorporating physical modeling could narrow down this spread. Despite this variability, the nominal model is sufficient to estimate the pinch-off time, with an error limited to a few instants. The resulting truncated firing waveform effectively excites the ECM, simulating volume growth that closely aligns with the experimental data with few fluctuations, see Fig. 7(a). The ECM can accurately estimate the grown drop volume at pinch-off, achieving a mean error of 0.15%. With volume adjustments, the mean of estimated in-flight drop volumes is 17.74 nl, with a 6.20% mean error compared to the measurement.

Fig. 7(b) demonstrates that the ECM can capture the development of average velocity adequately. With velocity compensation, the mean of estimated drop jetting velocities comes to 1.12 m/s, which is close to the mean of measured values of 1.05 m/s.

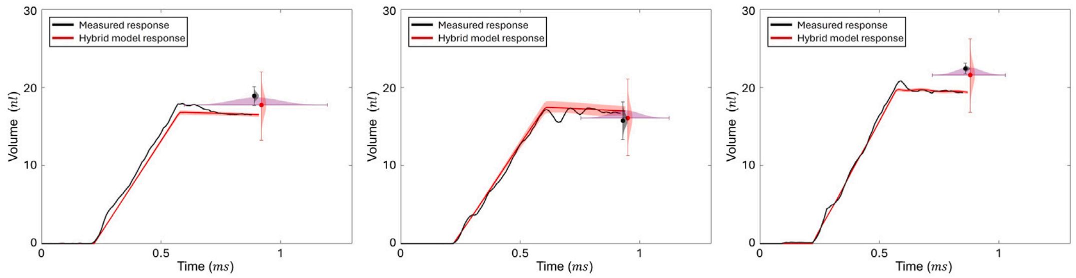

(a) Color ink: volume.

(c) DI water: volume.

(e) GW mixture: volume.

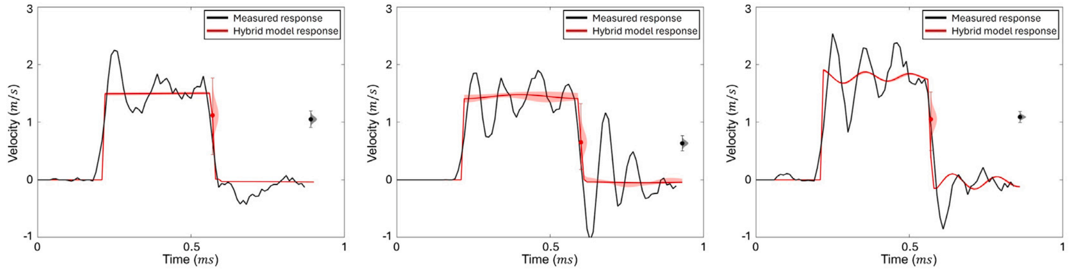

(b) Color ink: velocity.

(d) DI water: velocity.

(f) GW mixture: velocity.

Fig. 7. Comparison of the experimental and model-simulated drop volumes and velocities for color ink at (u_1 = 70 μm/ms, u_2 = 25 μm), DI water at (u_1 = 65 μm/ms, u_2 = 25 μm), and GW mixture at (u_1 = 85 μm/ms, u_2 = 30 μm), respectively. Black solid lines are the measured growing drop volumes and average velocities before pinch-off. Shaded red solid lines are the growing drop volumes and average velocities simulated by the uncertain ECMs. Black dots with shades denote the means of measured in-flight drop volumes and jetting velocities with their respective spreads. Red dots with shades are the means of in-flight drop volumes and jetting velocities simulated by the uncertain hybrid models with their respective spreads. Purple shades are the spreads of pinch-off instants.

5.3. Validation with data of other inks

Data of DI water collected at control parameters (u_1 = 65 μm/ms, u_2 = 25 μm) and GW mixture at (u_1 = 85 μm/ms, u_2 = 30 μm) are used to validate the hybrid modeling framework. Their properties are listed in Table 1, including densities, viscosities, and surface tensions commonly used in DoD inkjet printing. Following the modeling strategy outlined in Section 3, hybrid models for DI water and GW mixture are constructed and simulated based on the setup described in Section 5.1. Figs. 7(c) and 7(e) illustrate that the ECM responses show good agreement with experimental data. With volume adjustments, the mean errors are 2.13% for DI water and 3.65% for GW mixture, compared to the measured in-flight drop volume.

Figs. 7(d) and 7(f) compare the estimated jetting velocities with experimental measurements. The mean errors for both inks are within 4%, demonstrating the efficiency of the proposed modeling framework in estimating drop jetting velocity.

6. Conclusion

This paper proposes a physics-informed hybrid framework for modeling the formation of drop volume and jetting velocity in drop-on-demand inkjet printing. The framework integrates linear-time-invariant equivalent circuit models with linear adjusters and is validated with three different inks. Good agreement between Monte Carlo simulations and experimental data confirms the effectiveness of the framework. Furthermore, this framework characterizes an end-to-end linear-time-invariant relationship between in-flight drop volume and jetting velocity (the two desired output characteristics) and manufacturer-provided control parameters (the user-accessible input variables) with uncertain model parameters. This suggests the potential of using its static representation with uncertain model parameters for developing drop control strategies. The validated 3^{rd}– order ECM within the framework additionally can be employed to investigate printhead behaviors and design drop firing waveforms.

CRediT authorship contribution statement

Jie Wang: Writing – original draft, Visualization, Validation, Software, Methodology, Investigation, Formal analysis, Data curation, Conceptualization. **George T.-C. Chiu:** Writing – review & editing, Supervision, Conceptualization.

Declaration of competing interest

The authors declare that they have no known competing financial interests or personal relationships that could have appeared to influence the work reported in this paper.

Data availability

Data will be made available on request.

References

[1] A. Lu, J. Zhang, J. Jiang, Y. Zhang, B.R. Giri, V.R. Kulkarni, N.H. Aghda, J. Wang, M. Maniruzzaman, Novel 3D printed modular tablets containing multiple anti-viral drugs: a case of high precision drop-on-demand drug deposition, Pharm. Res. 39 (11) (2022) 2905–2918, http://dx.doi.org/10.1007/s11095-022-03378-9.

[2] M. Fligge, I. Letofsky-Papst, M. Bäumers, A. Zimmer, J. Breitkreutz, Personalized dermal patches – Inkjet printing of prednisolone nanosuspensions for individualized treatment of skin diseases, Int. J. Pharm. 630 (2023) 122382, http://dx.doi.org/10.1016/j.ijpharm.2022.122382.

[3] J. Lee, K. van der Maaden, G. Gooris, C. O'Mahony, W. Jiskoot, J. Bouwstra, Engineering of an automated nano-droplet dispensing system for fabrication of antigen-loaded dissolving microneedle arrays, Int. J. Pharm. 600 (2021) 120473, http://dx.doi.org/10.1016/j.ijpharm.2021.120473.

[4] W. Kamal, M. Li, J.-D. Lin, E. Parry, Y. Jin, S.J. Elston, A.A. Castrejón-Pita, S.M. Morris, Spatially patterned polymer dispersed liquid crystals for image-integrated smart windows, Adv. Opt. Mater. 10 (3) (2022) 2101748, http://dx.doi.org/10.1002/adom.202101748.

[5] A. Queraltó, J. Banchewski, A. Pacheco, K. Gupta, L. Saltarelli, D. Garcia, N. Alcalde, C. Mocuta, S. Ricart, F. Pino, X. Obradors, T. Puig, Combinatorial screening of cuprate superconductors by drop-on-demand inkjet printing, ACS Appl. Mater. Interfaces 13 (7) (2021) 9101–9112, http://dx.doi.org/10.1021/acsami.0c18014.

[6] M. Cirelli, J. Hao, T.C. Bor, J. Duvigneau, N. Benson, R. Akkerman, M.A. Hempenius, G.J. Vancso, Printing "smart" inks of redox-responsive organometallic polymers on microelectrode arrays for molecular sensing, ACS Appl. Mater. Interfaces 11 (40) (2019) 37060–37068, http://dx.doi.org/10.1021/acsami.9b11927.

[7] N. Bajaj, N.C. Giampietro, K. Mao, M.E. Rushton, N.A. Spomer, J.F. Rhoads, Searching for bed bugs: The design, development, and evaluation of an oscillator-based trans-2-hexenal sensor array, Sensors Actuators B 333 (2021) 129161, http://dx.doi.org/10.1016/j.snb.2020.129161.

[8] Y. Wu, G. Chiu, An improved model of height profile for drop-on-demand print of ultraviolet curable ink, ASME Lett. Dynam. Syst. Control 1 (3) (2021) 031010, http://dx.doi.org/10.1115/1.4050012.

[9] K. Tröndle, L. Rizzo, R. Pichler, F. Koch, A. Itani, R. Zengerle, S.S. Lienkamp, P. Koltay, S. Zimmermann, Scalable fabrication of renal spheroids and nephron-like tubules by bioprinting and controlled self-assembly of epithelial cells, Biofabrication 13 (3) (2021) 035019, http://dx.doi.org/10.1088/1758-5090/abe185.

[10] Y. Wu, G. Chiu, Error diffusion based feedforward height control for inkjet 3D printing, in: 2023 IEEE/ASME International Conference on Advanced Intelligent Mechatronics, AIM, 2023, pp. 125–131, http://dx.doi.org/10.1109/AIM46323.2023.10196116.

[11] H.Y. Gan, X. Shan, T. Eriksson, B.K. Lok, Y.C. Lam, Reduction of droplet volume by controlling actuating waveforms in inkjet printing for micro-pattern formation, J. Micromech. Microeng. 19 (5) (2009) 055010, http://dx.doi.org/10.1088/0960-1317/19/5/055010.

[12] Y. Liu, B. Derby, Experimental study of the parameters for stable drop-on-demand inkjet performance, Phys. Fluids 31 (3) (2019) 032004, http://dx.doi.org/10.1063/1.5085868.

[13] A.H. Hamad, M.I. Salman, A. Mian, Effect of driving waveform on size and velocity of generated droplets of nanosilver ink (Smartink), Manuf. Lett. 24 (2020) 14–18, http://dx.doi.org/10.1016/j.mfglet.2020.03.001.

[14] Y.-L. Cheng, T.-W. Tseng, Study on driving waveform design process for multi-nozzle piezoelectric printhead in material-jetting 3D printing, Rapid Prototyp. J. 27 (6) (2021) 1172–1180, http://dx.doi.org/10.1108/RPJ-05-2019-0120.

[15] T. Jiao, Q. Lian, T. Zhao, H. Wang, Influence of ink properties and voltage parameters on piezoelectric inkjet droplet formation, Appl. Phys. A 127 (1) (2021) 11, http://dx.doi.org/10.1007/s00339-020-04151-8.

[16] H. Wei, X. Xiao, Z. Yin, M. Yi, H. Zou, A waveform design method for high DPI piezoelectric inkjet print-head based on numerical simulation, Microsyst. Technol. 23 (12) (2017) 5365–5373, http://dx.doi.org/10.1007/s00542-017-3301-4.

[17] A.B. Aqeel, M. Mohasan, P. Lv, Y. Yang, H. Duan, Effects of the actuation waveform on the drop size reduction in drop-on-demand inkjet printing, Acta Mech. Sin. 36 (5) (2020) 983–989, http://dx.doi.org/10.1007/s10409-020-00991-y.

[18] H. Wang, Y. Hasegawa, Multi-objective optimization of actuation waveform for high-precision drop-on-demand inkjet printing, Phys. Fluids 35 (1) (2023) 013318, http://dx.doi.org/10.1063/5.0122124.

[19] M. Ezzeldin, P. van den Bosch, S. Weiland, Experimental-based feedforward control for a DoD inkjet printhead, Control Eng. Pract. 21 (7) (2013) 940–952, http://dx.doi.org/10.1016/j.conengprac.2013.03.002.

[20] D.B. Bogy, F.E. Talke, Experimental and theoretical study of wave propagation phenomena in drop-on-demand ink jet devices, IBM J. Res. Dev. 28 (3) (1984) 314–321, http://dx.doi.org/10.1147/rd.283.0314.

[21] K.-S. Kwon, W. Kim, A waveform design method for high-speed inkjet printing based on self-sensing measurement, Sensors Actuators A 140 (1) (2007) 75–83, http://dx.doi.org/10.1016/j.sna.2007.06.010.

[22] A.A. Khalate, X. Bombois, R. Babuška, H. Wijshoff, R. Waarsing, Performance improvement of a drop-on-demand inkjet printhead using an optimization-based feedforward control method, Control Eng. Pract. 19 (8) (2011) 771–781, http://dx.doi.org/10.1016/j.conengprac.2011.02.007.

[23] A.A. Khalate, X. Bombois, G. Scorletti, R. Babuska, S. Koekebakker, W. de Zeeuw, A waveform design method for a piezo inkjet printhead based on robust feedforward control, J. Microelectromech. Syst. 21 (6) (2012) 1365–1374, http://dx.doi.org/10.1109/JMEMS.2012.2205899.

[24] K. Wang, J. Xi, Optimization of the driving waveform of a piezoelectric inkjet printhead based on a system dynamics model, Rapid Prototyp. J. 24 (8) (2018) 1272–1280, http://dx.doi.org/10.1108/RPJ-05-2017-0102.

[25] A. Bsoul, S. Pan, E. Cretu, B. Stoeber, K. Walus, Design, microfabrication, and characterization of a moulded PDMS/SU-8 inkjet dispenser for a Lab-on-a-printer platform technology with disposable microfluidic chip, Lab Chip 16 (17) (2016) 3351–3361, http://dx.doi.org/10.1039/C6LC00636A.

[26] J. Wang, G.T.-C. Chiu, Control of drop volume and drop jetting velocity in inkjet printing, IFAC-PapersOnLine 55 (27) (2022) 37–43, http://dx.doi.org/10.1016/j.ifacol.2022.10.485, 9th IFAC Symposium on Mechatronic Systems MECHATRONICS 2022.

[27] T. Wang, T.-H. Kwok, C. Zhou, S. Vader, In-situ droplet inspection and closed-loop control system using machine learning for liquid metal jet printing, J. Manuf. Syst. 47 (2018) 83–92, http://dx.doi.org/10.1016/j.jmsy.2018.04.003.

[28] J. Wang, X. Chen, G. Chiu, Drop volume control in drop-on-demand inkjet printing, in: Proc. ASME Dyn. Syst. Control Conf. (DSCC2019), 2019, http://dx.doi.org/10.1115/DSCC2019-9233, V003T17A011.

[29] J. Wang, G.T.-C. Chiu, Control of on-demand nanoliter drop volume and jetting velocity in piezoelectric inkjet printing, Mechatronics 94 (2023) 103031, http://dx.doi.org/10.1016/j.mechatronics.2023.103031.

[30] J. Wang, G.T.-C. Chiu, Drop-on-demand inkjet drop control with one-step look ahead estimation of model parameters, IEEE/ASME Trans. Mechatronics 28 (4) (2023) 1993–2002, http://dx.doi.org/10.1109/TMECH.2023.3277455.

[31] X. Yue, J. Chen, H. Yang, X. Li, J. Xiong, Z. Yin, Multinozzle droplet volume distribution control in inkjet printing based on multiagent soft actor–critic network, IEEE/ASME Trans. Mechatronics (2024) 1–11, http://dx.doi.org/10.1109/TMECH.2024.3401015.

[32] J. Fromm, Numerical calculation of the fluid dynamics of drop-on-demand jets, IBM J. Res. Dev. 28 (3) (1984) 322–333, http://dx.doi.org/10.1147/rd.283.0322.

[33] Q. Xu, O. Basaran, Computational analysis of drop-on-demand drop formation, Phys. Fluids 19 (10) (2007) 102111, http://dx.doi.org/10.1063/1.2800784.

[34] J. de Jong, R. Jeurissen, H. Borel, M. van den Berg, H. Wijshoff, H. Reinten, M. Versluis, A. Prosperetti, D. Lohse, Entrapped air bubbles in piezo-driven inkjet printing: Their effect on the droplet velocity, Phys. Fluids 18 (12) (2006) 121511, http://dx.doi.org/10.1063/1.2397015.

[35] D. Shin, P. Smith, Theoretical investigation of the influence of nozzle diameter variation on the fabrication of thin film transistor liquid crystal display color filters, J. Appl. Phys. 103 (11) (2008) http://dx.doi.org/10.1063/1.2936885.

[36] Y. Mao, X. Wang, X. Li, B. Li, J. Chu, Modelling on the droplet formation and optimizing of the microfluidic cartridge used for the microfluidic impact printing, J. Micromech. Microeng. 29 (12) (2019) http://dx.doi.org/10.1088/1361-6439/ab4cda.

[37] M.A. Shah, D.-G. Lee, S. Hur, Design and characteristic analysis of a MEMS piezo-driven recirculating inkjet printhead using lumped element modeling, Micromachines 10 (11) (2019) http://dx.doi.org/10.3390/mi10110757.

[38] Y. Yoshida, K. Izumi, H. Ushijima, Nonlinear piezo-inkjet equivalent circuit modeling for predicting ink ejection velocity fluctuation caused by meniscus oscillation, AIP Adv. 10 (6) (2020) 065025, http://dx.doi.org/10.1063/5.0011664.

[39] J. Wang, C. Xiong, J. Huang, J. Peng, J. Zhang, P. Zhao, Waveform design method for piezoelectric print-head based on iterative learning and equivalent circuit model, Micromachines 14 (4) (2023) http://dx.doi.org/10.3390/mi14040768.

[40] Q. Gallas, R. Holman, T. Nishida, B. Carroll, M. Sheplak, L. Cattafesta, Lumped element modeling of piezoelectric-driven synthetic jet actuators, AIAA J. 41 (2) (2003) 240–247, http://dx.doi.org/10.2514/2.1936.

[41] J. Shi, B. Wu, B. Song, J. Song, S. Li, D. Trau, W.F. Lu, Learning-based cell injection control for precise drop-on-demand cell printing, Ann. Biomed. Eng. 46 (9) (2018) 1267–1279, http://dx.doi.org/10.1007/s10439-018-2054-2.

[42] J. Huang, L.J. Segura, T. Wang, G. Zhao, H. Sun, C. Zhou, Unsupervised learning for the droplet evolution prediction and process dynamics understanding in inkjet printing, Addit. Manuf. 35 (2020) 101197, http://dx.doi.org/10.1016/j.addma.2020.101197.

[43] L.J. Segura, Z. Li, C. Zhou, H. Sun, Droplet evolution prediction in material jetting via tensor time series analysis, Addit. Manuf. 66 (2023) 103461, http://dx.doi.org/10.1016/j.addma.2023.103461.

[44] D. Wu, C. Xu, Predictive modeling of droplet formation processes in inkjet-based bioprinting, J. Manuf. Sci. Eng. 140 (10) (2018) 101007, http://dx.doi.org/10.1115/1.4040619.

[45] F.P. Brishty, R. Urner, G. Grau, Machine learning based data driven inkjet printed electronics: jetting prediction for novel inks, Flex. Print. Electron. 7 (1) (2022) 015009, http://dx.doi.org/10.1088/2058-8585/ac5a39.

[46] S. Kim, M. Cho, S. Jung, The design of an inkjet drive waveform using machine learning, Sci. Rep. 12 (1) (2022) 4841, http://dx.doi.org/10.1038/s41598-022-08784-y.

[47] S. Kim, R. Wenger, O. Bürgy, G. Balestra, U. Jeong, S. Jung, Predicting inkjet jetting behavior for viscoelastic inks using machine learning, Flex. Print. Electron. 8 (3) (2023) 035007, http://dx.doi.org/10.1088/2058-8585/acee94.

[48] D. Garcia, Z. Wu, J.Y. Kim, H.Z. Yu, Y. Zhu, Heterogeneous materials design in additive manufacturing: Model calibration and uncertainty-guided model selection, Addit. Manuf. 27 (2019) 61–71, http://dx.doi.org/10.1016/j.addma.2019.02.014.

[49] I.A. Spiegel, P. Sammons, K. Barton, Hybrid modeling of electrohydrodynamic jet printing, IEEE Trans. Control Syst. Technol. 28 (6) (2020) 2322–2335, http://dx.doi.org/10.1109/TCST.2019.2939963.

[50] T. Moges, Z. Yang, K. Jones, S. Feng, P. Witherell, Y. Lu, Hybrid modeling approach for melt-pool prediction in laser powder bed fusion additive manufacturing, J. Comput. Inf. Sci. Eng. 21 (5) (2021) 050902, http://dx.doi.org/10.1115/1.4050044.

[51] B. Mondal, T. Mukherjee, T. DebRoy, Crack free metal printing using physics informed machine learning, Acta Mater. 226 (2022) 117612, http://dx.doi.org/10.1016/j.actamat.2021.117612.

[52] J. Wang, G.T.-C. Chiu, Data-driven drop formation modeling in nanoliter drop-on-demand inkjet printing, in: Proc. ASME Dyn. Syst. Control Conf. (DSCC2020), 2020, http://dx.doi.org/10.1115/DSCC2020-3292, V002T28A002.

[53] J.Q. Feng, A general fluid dynamic analysis of drop ejection in drop-on-demand ink jet devices, J. Imaging Sci. Technol. 46 (5) (2002) 398–408.

[54] X. Wang, W.W. Carr, D.G. Bucknall, J.F. Morris, Drop-on-demand drop formation of colloidal suspensions, Int. J. Multiph. Flow 38 (1) (2012) 17–26, http://dx.doi.org/10.1016/j.ijmultiphaseflow.2011.09.001.

[55] J.R. Castrejón-Pita, A.A. Castrejón-Pita, S.S. Thete, K. Sambath, I.M. Hutchings, J. Hinch, J.R. Lister, O.A. Basaran, Plethora of transitions during breakup of liquid filaments, Proc. Natl. Acad. Sci. 112 (15) (2015) 4582–4587, http://dx.doi.org/10.1073/pnas.1418541112.

[56] M.L. Eggersdorfer, H. Seybold, A. Ofner, D.A. Weitz, A.R. Studart, Wetting controls of droplet formation in step emulsification, Proc. Natl. Acad. Sci. 115 (38) (2018) 9479–9484, http://dx.doi.org/10.1073/pnas.1803644115.

[57] D. Lohse, Fundamental fluid dynamics challenges in inkjet printing, Annu. Rev. Fluid Mech. 54 (1) (2022) 349–382, http://dx.doi.org/10.1146/annurev-fluid-022321-114001.

[58] S. Kandlikar, S. Garimella, D. Li, S. Colin, M.R. King, Heat transfer and fluid flow in minichannels and microchannels, in: Heat Transfer and Fluid Flow in Minichannels and Microchannels, second ed., Butterworth-Heinemann, Oxford, 2014.

[59] K.W. Oh, K. Lee, B. Ahn, E.P. Furlani, Design of pressure-driven microfluidic networks using electric circuit analogy, Lab Chip 12 (3) (2012) 515–545, http://dx.doi.org/10.1039/C2LC20799K.

[60] J.S. Armstrong, Principles of Forecasting: a Handbook for Researchers and Practitioners, vol. 30, Springer, 2001.

[61] H. Garnier, M. Mensler, A. Richard, Continuous-time model identification from sampled data: Implementation issues and performance evaluation, Internat. J. Control 76 (13) (2003) 1337–1357, http://dx.doi.org/10.1080/0020717031000149636.

[62] H. Garnier, L. Wang, P.C. Young, Direct identification of continuous-time models from sampled data: Issues, basic solutions and relevance, in: Identification of Continuous-Time Models from Sampled Data, Springer London, London, 2008, pp. 1–29, http://dx.doi.org/10.1007/978-1-84800-161-9_1.

[63] G. Goodwin, R. Middleton, H. Poor, High-speed digital signal processing and control, Proc. IEEE 80 (2) (1992) 240–259, http://dx.doi.org/10.1109/5.123294.